Research Letter

How to Cite: *J. Inorg. Mater.*, 2026, **41(6):** 839
DOI: 10.15541/jim20250319

Enhanced ROS Scavenging Property of Polyoxometalates by Manganese Doping for Cytoprotection

QU Boxuan[1,2], TAN Ji[1], CHEN Shuhan[1], LIU Xuanyong[1]

(1. State Key Laboratory of High Performance Ceramics, Shanghai Institute of Ceramics, Chinese Academy of Sciences, Shanghai 200050, China; 2. Center of Materials Science and Optoelectronics Engineering, University of Chinese Academy of Sciences, Beijing 100049, China)

Abstract: Excessive accumulation of reactive oxygen species (ROS) can trigger oxidative stress in cells, ultimately leading to cell death. Nanozymes, a class of nanomaterials with enzyme-like catalytic activity, are capable of scavenging ROS and protecting cells from oxidative damage. Polyoxometalates (POMs), known for their favorable redox properties and biocompatibility, have been considered as potential nanozyme candidates. However, their relatively low catalytic activity has hindered their practical applications. In this study, an isomorphic doping strategy with manganese (Mn) was employed to effectively enhance the enzyme-like activity of Keggin-type POMs ($[PMo_{12}O_{40}]^{3-}$). It was found that appropriate Mn doping significantly improved both the catalase-like (CAT-like) and superoxide dismutase-like (SOD-like) activities of the POMs, thereby enhancing its ability to eliminate excessive ROS and protect cells from oxidative stress-induced damage. The relationships among Mn doping levels, POMs structure, and catalytic activity were systematically investigated. The results suggest that the synergistic electronic interaction between Mn and Mo–O framework plays a crucial role in enhancing the CAT-like activity of the material. This work provides a preliminary exploration of design strategies for POMs-based nanozymes and offers scientific insights for the development of antioxidant nanozymes.

Key words: polyoxometalate; oxidative stress; nanozyme; catalytic medicine

Oxidative stress, an imbalance between reactive oxygen species (ROS) and antioxidant defenses, poses a significant threat to cellular health and is implicated in various diseases, including neurodegenerative disorders and cancer[1]. Due to their higher stability and tunability compared to natural enzymes, nanozymes have emerged as promising therapeutic agents for mitigating oxidative stress[2].

Polyoxometalates (POMs) are a class of inorganic metal-oxide clusters composed of transition metals (*e.g.*, V, Mo, and W) linked together by shared oxygen atoms. They offer a unique combination of properties, including high biocompatibility, facile permeation, and redox activity, making them attractive candidates for developing novel nanozymes[3]. Nevertheless, the catalytic ability of POMs to scavenge ROS is limited. Ion doping can adjust the structural and electronic properties of materials, thereby influencing their catalytic performance[4-5]. Previous studies have shown that incorporating foreign atoms into P_8W_{48} POMs enhances their catalytic-like activity[6]. Manganese (Mn) is a metal center in some redox enzymes and is commonly used to enhance the enzymatic activity of nanozymes. However, it remains unclear how Mn doping modulates the electronic structure of POMs and thereby governs their enzyme-like activities.

This study focuses on the synthesis and characterization of Mn-doped POMs to enhance their antioxidant enzyme-like activities. The relationship between Mn doping, structural properties and their impact on enzymatic activities was investigated. Mn-doped POMs exhibited potent antioxidant capabilities, effectively scavenging intracellular ROS and alleviating oxidative stress. This study provides a new paradigm for designing POM-based nanozymes for the treatment of ROS-related diseases.

Received date: 2025-07-30; **Revised date:** 2025-09-22; **Published online:** 2026-05-29
Foundation item: National Key Research and Development Program of China (2022YFC2403000)
Biography: QU Boxuan (1998–), male, Master candidate. E-mail: quboxuan@mail.ustc.edu.cn
曲博渲(1998–), 男, 硕士研究生. E-mail: quboxuan@mail.ustc.edu.cn
Corresponding author: TAN Ji, associate professor. E-mail: tanji@mail.sic.ac.cn; LIU Xuanyong, professor. E-mail: xyliu@mail.sic.ac.cn
谭 继, 副研究员. E-mail: tanji@mail.sic.ac.cn; 刘宣勇, 研究员. E-mail: xyliu@mail.sic.ac.cn

1 Experimental

1.1 Chemicals

Hexaammonium molybdate tetrahydrate ($(NH_4)_6Mo_7O_{24}\cdot 4H_2O$), sodium dihydrogen phosphate dodecahydrate ($NaH_2PO_4\cdot 12H_2O$) and manganese (II) acetate tetrahydrate ($Mn(CH_3COO)_2\cdot 4H_2O$) were purchased from Aladdin Reagent Co., Ltd. Hydrogen peroxide (H_2O_2, 30% (in mass)), titanium (IV) sulfate ($Ti(SO_4)_2$), and ethanol (C_2H_5OH) were obtained from Sinopharm Chemical Reagent Co., Ltd. (Shanghai, China). All chemicals were analytical grade and used directly without further purification. All aqueous solutions were prepared with ultrapure water (18.2 MΩ·cm, Millipore).

1.2 Preparation of POM-Mn*x*

POM-Mn*x* was synthesized using traditional methods[7]. Briefly, 0.2 mmol of POM cluster was dissolved in 2 mL of water, and 100, 500 or 2000 μL of 0.2 mol/L Mn acetate were added. After stirring for 10 min, the clusters were precipitated by adding 10 mL of ethanol, collected by centrifugation, washed three times with water and ethanol, and finally lyophilized. Based on the Mn-to-POM ratio, the samples (POM-Mn*x*, *x* represents the Mn/POM molar ratio) are designated as POM-Mn0.1, POM-Mn0.5 and POM-Mn2.0.

1.3 Characterization methods

Morphological studies were carried out using a Tecnai G2 F20 transmission electron microscope (TEM, Shimadzu, Japan) at an acceleration voltage of 200 kV. Crystal structures of samples were analyzed using an X-ray diffractometer (XRD, Bruker D8, Germany). Fourier transform infrared (FT-IR) characterization was performed on a Fourier transform infrared spectrometer (Bruker Tensor 27, Germany). Raman scattering was conducted on the HORIBA Jobin Yvon HR800. The manganese content was analyzed by inductively coupled plasma optical emission spectrometry (ICP-OES, Agilent 725, USA). All colorimetric and fluorescent tests were conducted using a multi-functional microplate reader (Cytation5, BioTec, USA).

1.4 CAT-like activity measurements

CAT-like activity of POM-Mn*x* was determined by monitoring the amount of oxygen generated within 5 min using a dissolved oxygen meter. Specifically, H_2O_2 and POM-Mn*x* were mixed in phosphate buffer solution (PBS, pH 7.4, 20 mmol/L) to a total volume of 2 mL. The final concentrations of H_2O_2 and POM-Mn*x* were 100 mmol/L and 1 mg/mL, respectively.

POM-Mn*x* (100 μL, 1 mg/mL) and H_2O_2 (100 μL, 3 mmol/L) were added to PBS (pH 7.4, 20 mmol/L) to make a total volume of 1 mL. The mixture was incubated at 37 ℃ for 6 h. After incubation, 200 μL of the reaction solution was mixed with 20 μL of 1% (in mass) $Ti(SO_4)_2$ solution and left to react for 5 min. The absorbance of the solution at 405 nm was then measured using a multi-functional microplate reader. H_2O_2 scavenging efficiency was calculated as the following formula:

$$\text{Scavenging efficiency} = \frac{A\text{o} - A\text{n}}{A\text{p} - A\text{n}} \times 100\% \quad (1)$$

where *A*o, *A*n, and *A*p are the absorbance of the treated samples, negative control, and positive control, respectively.

1.5 SOD-like activity measurements

SOD-like activity of POM-Mn*x* was evaluated using the total superoxide dismutase assay kit with WST-8 (S0101M, Beyotime). The $\cdot O_2^-$ scavenging efficiency was calculated using the same formula as that for H_2O_2 scavenging efficiency.

1.6 EDTA inhibition of POM-Mn*x*

To evaluate the inhibitory effect of ethylenediamine tetraacetic acid (EDTA) on POM-Mn*x* CAT-like activity, 100 mg/L EDTA was introduced into the reaction system. Specifically, POM-Mn*x* (100 μL, 1 mg/mL), H_2O_2 (100 μL, 3 mmol/L), and EDTA (100 μL, 100 mg/L) were added to PBS (pH 7.4, 20 mmol/L) to reach a total volume of 1 mL. The mixture was incubated at 37 ℃ for 5 h. After incubation, 200 μL of the reaction solution was mixed with 20 μL of 1% (in mass) $Ti(SO_4)_2$ solution and allowed to react for 5 min. The absorbance at 405 nm was then measured using a multi-functional microplate reader.

1.7 Cell culture

Macrophages (RAW264.7) were obtained from the Cell Bank of the Chinese Academy of Sciences (Shanghai, China). RAW246.7 cells were cultured in high-glucose Dulbecco's modified Eagle medium (DMEM, high glucose, Gibco, USA) supplemented with 1% penicillin-streptomycin and 15% (in volume) fetal bovine serum (FBS) in a humidified atmosphere of 5% CO_2 at 37 ℃.

1.8 Cell viability

Cell viability was measured using the AlamarBlue™ assay (Thermo Fisher Scientific, USA) to evaluate the cytotoxicity and antioxidative effects of POM-Mn*x*. RAW264.7 cells were seeded at 1×10^4 cells per well in 96-well white cell culture plates and incubated at 37 ℃ for 24 h. For antioxidation assays, RAW264.7 cells were seeded at 3×10^4 cells per well in 96-well plates, and culture media containing various concentrations of POM, POM-Mn0.1, POM-Mn0.5, and POM-Mn2.0, along with 1000 μmol/L H_2O_2, was added to the wells and incubated for 6 h. After incubation, the culture medium was discarded, and cell viability was assessed using the AlamarBlue™ assay. Biocompatibility assays followed similar steps without the addition of H_2O_2, and the incubation time was extended to 24 h.

1.9　Live/dead cell staining

Live/dead cell staining was performed using the live/dead cell staining kit (Biovision, USA) to evaluate the cytotoxicity and antioxidative effects of POM-Mn*x*. RAW264.7 cells were seeded in 24-well plates and incubated at 37 ℃ for 24 h. For antioxidation assays, the cells were treated for 6 h with culture media containing 1000 μmol/L H_2O_2 and 100 μg/mL of POM, POM-Mn0.1, POM-Mn0.5, or POM-Mn2.0. Subsequently, the cells were stained for 30 min with calcein AM (green, staining live cells) and propidium iodide (PI, red, staining dead and dying cells). Live and dead cells were observed using a fluorescence microscope (Olympus IX71, Japan). For cytotoxicity assays, the procedure was similar but without H_2O_2, and the treatment time was extended to 24 h.

1.10　Intracellular ROS detection

RAW264.7 cells were seeded in 24-well plates at a density of 100000 cells per well and incubated at 37 ℃ for 24 h. After removing the medium, the following treatments were applied: (1) control group with fresh medium; (2) 500 μmol/L H_2O_2; (3) to (6) 100 μg/mL POM-Mn*x* plus 500 μmol/L H_2O_2. The cells were then incubated at 37 ℃ for 6 h. Subsequently, 10 μmol/L 2′,7′-dichlorofluorescein diacetate (DCFH-DA, Sigma-Aldrich, Germany) was added to stain intracellular ROS, and the cells were incubated in the dark at 37 ℃ for 30 min. After staining, the cells were rinsed three times with PBS, and intracellular ROS were observed using fluorescence microscopy.

1.11　Statistical analysis

GraphPad Prism and Origin statistical software package were used to determine the statistical significance. Raman spectra were normalized using the min-max normalization method in Origin software. All data were described as mean±standard deviation (SD) by the analysis of three parallel samples.

2　Results and discussion

2.1　Synthesis and characterization of POM-Mn*x*

As illustrated in Fig. 1, Mn ions were introduced into the POM precursor solution to partially substitute Mo atoms, owing to their similar ionic radius and capacity for octahedral coordination. This substitution locally modulates the structure and electronic environment of the POM clusters. Ethanol was subsequently added to induce hydrogen bond-mediated aggregation, promoting the precipitation of POM-Mn*x*. The resulting precipitate was collected by centrifugation and freeze drying to yield the final solid product.

The quantitative relationship between Mn content and Mn-to-POM feed ratio, as presented in Fig. 2(a), highlights the successful incorporation of Mn into the POM matrix. The crystal structure of the samples was characterized by XRD, and the results are shown in Fig. 2(b). POM crystals are composed of POM clusters and cations. Undoped POM shows one peak in the range of 2θ=10°–15°, while POM-Mn*x* displays peaks in the range of 2θ=15°–17°, 20°–25° and 25°–32°, indicating mixed phases due to multiple isomeric forms in solution[8]. Fig. 2(c) shows TEM images of POM and POM-Mn0.5. Both POM and POM-Mn0.5 have a regular hexagonal structure, and doping does not significantly change particle size. This indicates that Mn doping does not cause drastic changes in the overall chemical structure of POM, and its influence may be limited to local regions. Raman analysis (Fig. 2(d)) shows peaks in the high wavenumber region for POM, POM-Mn0.1, and POM-Mn0.5 correspond to M=O (M: metal) double bond stretching vibrations (v=32895exp(–2.073R), where v and R represent Raman shift (cm^{-1}) and bond length (1.71, 1.70, and 1.78 Å), respectively)[9]. The peaks at low wavenumbers are attributed to O–M–O bending vibrations. POM-Mn2.0 shows an increased double bond length, suggesting electrons are closer to the Mo–O–Mo framework. This disrupted electron-sharing framework may affect catalytic performance. FT-IR spectroscopy (Fig. 2(e)) shows that doped POMs have higher vibration intensity than undoped POM. This is due to manganese disrupting the symmetry and creating asymmetrical bonds[10]. The P–O bond weakens with increased Mn doping, indicated by decreased absorption at 1040 cm^{-1}. The above results confirmed that POM-Mn*x* was successfully prepared. And with the increase of Mn doping ratio, there is a structural mutation when the Mn/POM molar ratio is 2.0, and the Mo=O double bond length decreases and transforms into a Mo–O single bond.

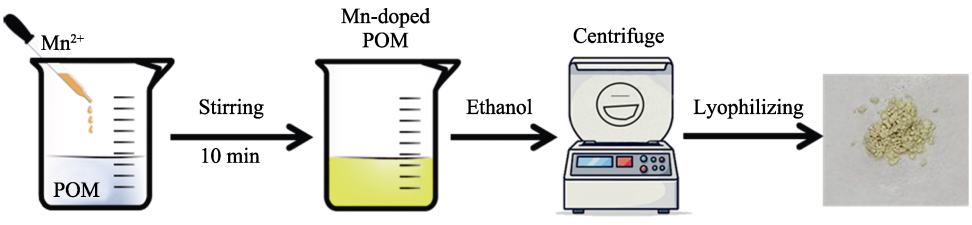

Fig. 1　Synthetic schematic of POM-Mn*x* samples

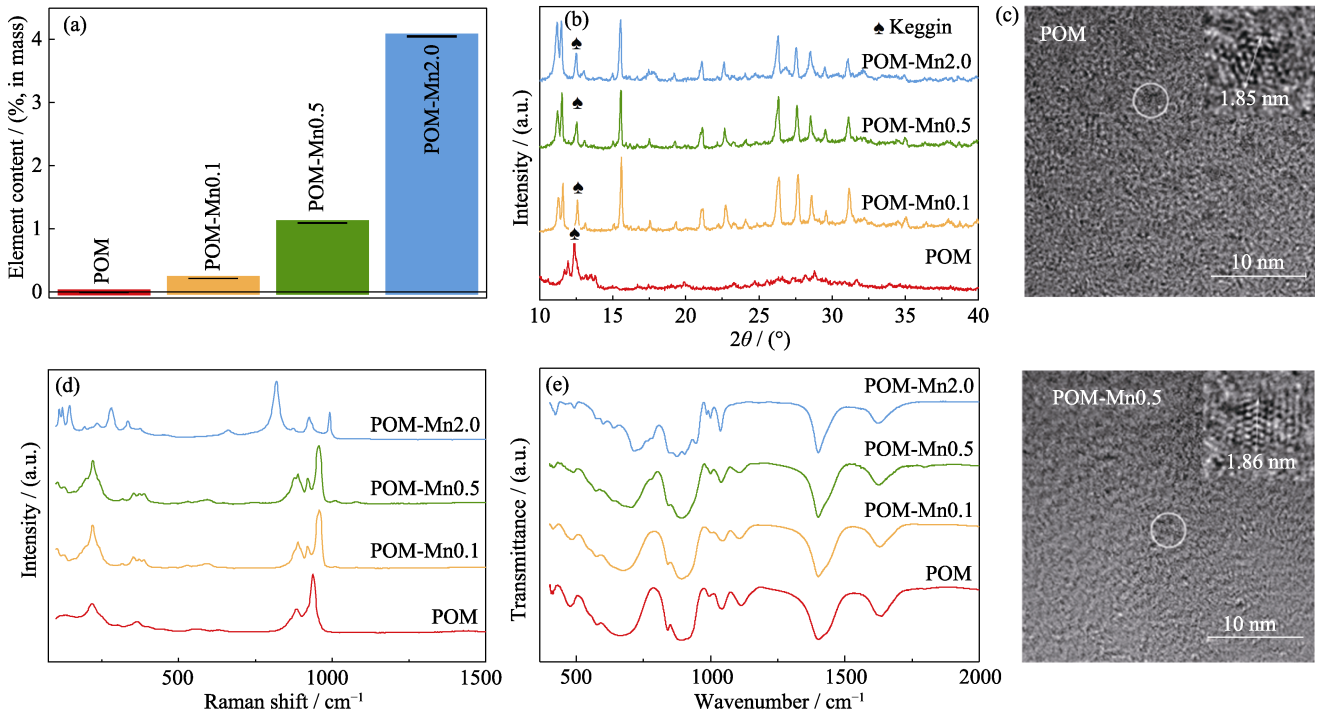

Fig. 2 (a) Mn content in POM-Mn*x* measured by ICP-OES; (b) XRD patterns, (c) TEM images, (d) Raman spectra, and (e) FT-IR spectra of POM-Mn*x* samples

The Mn2p XPS spectra of POM-Mn*x* samples are presented in Fig. 3(a). With an increasing Mn doping ratio, the average oxidation state of Mn gradually increases. These results indicate a shift in Mn oxidation state from Mn^{3+}-dominated to Mn^{4+}-dominated as the doping level increases.

Fig. 3(b) presents the UV-Vis absorption spectra of POM and POM-Mn*x* samples in the range of 250–2500 nm. Pristine POM exhibits a sharp absorption edge below 400 nm, attributed to an O→Mo charge transfer band. For POM-Mn0.1, the absorption edge remains largely unchanged, while a slight enhancement in the visible-near infrared (NIR) region is observed. Upon increasing the Mn doping level to POM-Mn0.5, the primary absorption edge becomes significantly less steep, and the long-wavelength absorption weakens overall. This suggests that Mn^{2+}/Mn^{3+} doping induces less distortion in the Mo–O framework symmetry, thereby reducing the density of states and suppressing optical transitions. In the highly doped POM-Mn2.0 sample, a distinct new absorption band emerges in the 500–1500 nm region (as indicated by the arrow), accompanied by a broad and shallow absorption tail spanning 800–1600 nm. These features indicate enhanced d-d transitions or intervalence charge transfer processes induced by Mn doping. This may result from partial oxidation of Mn to higher oxidation states (*e.g.*, Mn^{4+}) to maintain charge neutrality, where the incorporation of high-valent Mn–O polyhedra leads to orbital hybridization with Mo–O octahedra, generating new electronic transitions near 500 nm and intensifying NIR tail absorption.

In this study, the bandgaps of POM and POM-Mn*x* samples were estimated using Tauc plot analysis, which adopts classical semiconductor models as empirical tools for bandgap fitting and comparison. As shown in Fig. 3(c), POM, POM-Mn0.1 and POM-Mn0.5 exhibits good linearity when fitted using the direct transition model ($(\alpha h\nu)^2$–$h\nu$), indicating that their optical absorption behaviors can be approximated as direct transitions. In contrast, the heavily doped sample POM-Mn2.0 fails to yield a reasonable bandgap under the direct transition model, but shows much improved linearity when fitted with the indirect transition model ($(\alpha h\nu)^{1/2}$–$h\nu$), suggesting that it follows an indirect transition behavior. Based on these fittings, the estimated optical bandgaps of POM, POM-Mn0.1, POM-Mn0.5, and POM-Mn2.0 are 2.86, 1.46, 1.63, and 3.10 eV, respectively. It is important to note that POM-based materials are essentially molecular cluster systems with discrete energy levels, rather than extended band structures as found in conventional crystalline semiconductors. Therefore, the terms “direct” and “indirect” transitions here refer only to the mathematical models used for optical bandgap fitting, rather than implying actual physical processes involving the Brillouin zone or phonon participation.

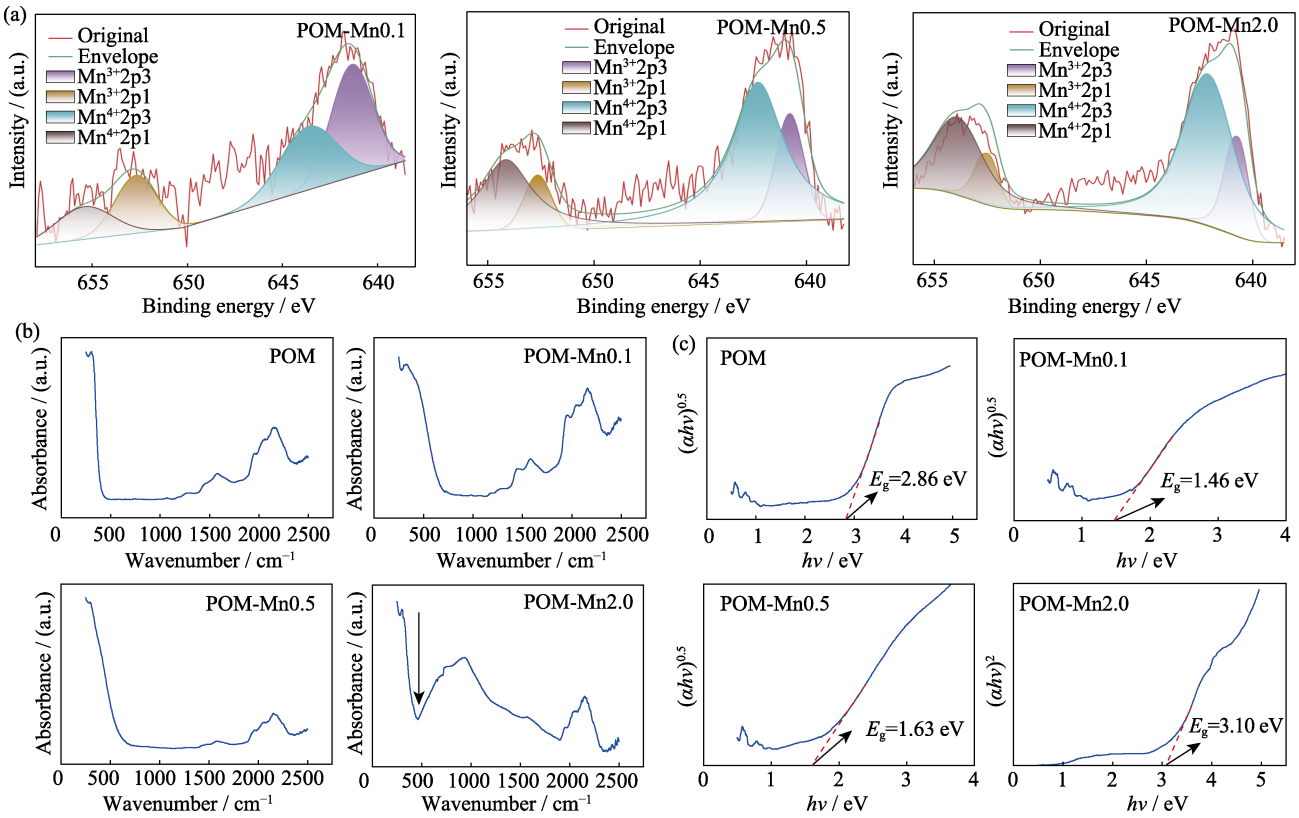

Fig. 3　(a) Mn2p XPS spectra of POM-Mn0.1, POM-Mn0.5 and POM-Mn2.0; (b) UV-Vis absorption spectra and (c) Tauc plots of POM, POM-Mn0.1, POM-Mn0.5 and POM-Mn2.0

2.2　Multiple enzyme-like activities of POM-Mn*x*

This study characterized materials with various doping levels and investigated the relationship between their CAT-like activity and doping amount.

Figs. 4(a, b) demonstrate that when the doping amount is less than 1.0, CAT-like activity increases with the increase in doping amount. Specifically, the CAT-like activities of POM, POM-Mn0.1, and POM-Mn0.5 are (33.24±0.55)%, (61.62±0.45)%, and (92.03±0.15)%, respectively. Among these samples, POM-Mn0.5 exhibits the highest CAT-like activity, while the CAT-like activity of POM-Mn2.0 abruptly drops to (45.36±2.34)%. These results indicate that appropriate doping can effectively enhance the CAT-like activity of POM. The generation of O_2 was directly measured (Fig. 4(c)), confirming that the POM-Mn*x* decompose hydrogen peroxide predominantly *via* CAT-like activity rather than through other catalytic pathways. Furthermore, a reduction in CAT-like activity is observed in conjunction with the structural transition, suggesting that changes in the POM framework may influence catalytic efficiency.

To investigate the catalytic active center, EDTA was introduced as a chelating agent for Mn ions, as shown in Fig. 4(d). Before EDTA treatment, the CAT-like activities of POM, POM-Mn0.1, POM-Mn0.5, and POM-Mn2.0 are (13.77±0.16)%, (36.86±0.73)%, (82.09±0.20)%, and (24.56±1.28)%, respectively. After EDTA addition, the activities decreased to (13.18±0.68)%, (9.43±0.24)%, (15.15±0.18)%, and (20.63±0.38)%, corresponding to relative reductions of 4.3%, 74.4%, 81.5%, and 16.0%, respectively. These results suggest that the CAT-like activity of POM-Mn0.1 and POM-Mn0.5 is highly dependent on the presence of Mn atoms, as evidenced by the substantial decline upon chelation. In contrast, POM and POM-Mn2.0 exhibit only minor reductions in activity, indicating that their catalytic performance is primarily derived from the intrinsic Mo–O framework rather than Mn centers. The relative insensitivity of POM-Mn2.0 to EDTA may be attributed to its structural transformation from Mo=O double bonds to Mo–O–Mo single bonds, which reduces the reliance on Mn as an active site. Although EDTA chelation may not be complete, the negligible effect on undoped POM confirms that the Mo–O matrix itself is catalytically competent and unaffected by chelation agents.

The SOD-like enzyme activity of nanozymes is shown in Figs. 4(e, f). Specifically, POM, POM-Mn0.1, POM-Mn0.5, and POM-Mn2.0 exhibit SOD-like activities of (27.04±1.77)%, (21.04±0.72)%, (87.30±0.15)%, and (83.54±2.82)%, respectively. When the doping amount is greater than or equal to 0.5, the SOD-like catalytic performance surges to more than four times the original.

This enhancement is attributed to the favorable distribution of Mn^{3+} and Mn^{4+} in POM-Mn0.5 and POM-Mn2.0, which supports the redox cycling required for effective superoxide dismutation[11].

The above results demonstrate that when the Mn/POM molar ratio is between 0.1 and 0.5, the CAT-like activity of POM is related to both Mn atoms and Mo=O double bonds, while the CAT-like activity of POM and POM-Mn2.0 comes from its Mo–O framework rather than Mn atoms. In contrast, the SOD-like activity is closely correlated with the redox behavior of Mn centers. In particular, the presence of both Mn^{3+} and Mn^{4+} in POM-Mn0.5 and POM-Mn2.0 forms a favorable redox pair that facilitates superoxide dismutation, leading to enhanced SOD-like catalytic performance.

2.3 Cytoprotection performance of POM-Mn*x*

POM-Mn*x* exhibits significant and stable $\cdot O_2^-$ scavenging ability and H_2O_2 decomposition ability under physiological conditions, which can remove excess ROS in a typical redox imbalance environment and protect cells from oxidative stress.

Firstly, the biocompatibility of POM-Mn*x* on RAW264.7 cells was investigated. As shown in Fig. 5, POM, POM-Mn0.1, and POM-Mn0.5 exhibit no obvious cytotoxicity, with RAW264.7 cells viability maintained above 80% across a concentration range of 100–300 mg/L. In contrast, POM-Mn2.0 showed a dose-dependent decrease in viability, with values of 77.49%, 73.67%, and 68.89% at

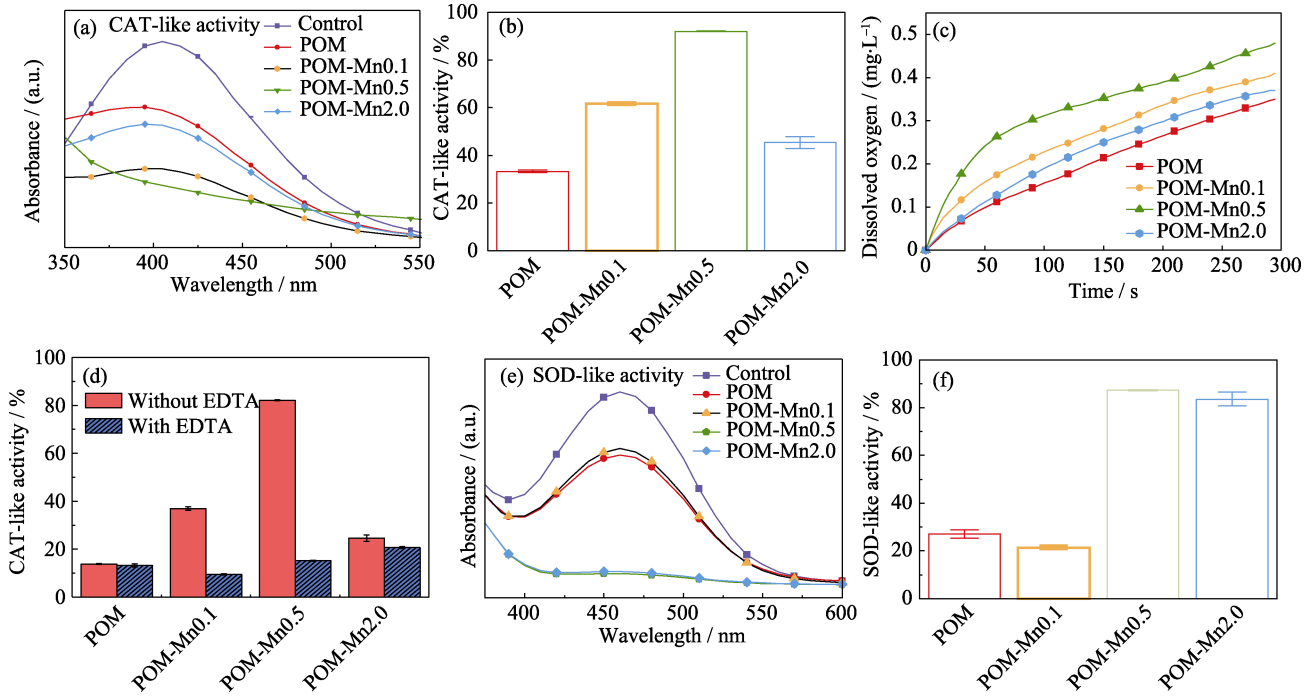

Fig. 4 (a) UV-Vis spectra of H_2O_2-$Ti(SO_4)_2$ colorimetric systems for the CAT-like activity assessment, (b) quantitative analysis of CAT-like activity, (c) dissolved oxygen generation curves, (d) CAT-like activity with or without EDTA chelation, (e) UV-Vis spectra of WST-formazan for the SOD-like activity assessment, and (f) quantitative analysis of SOD-like activity treated with POM, POM-Mn0.1, POM-Mn0.5, and POM-Mn2.0

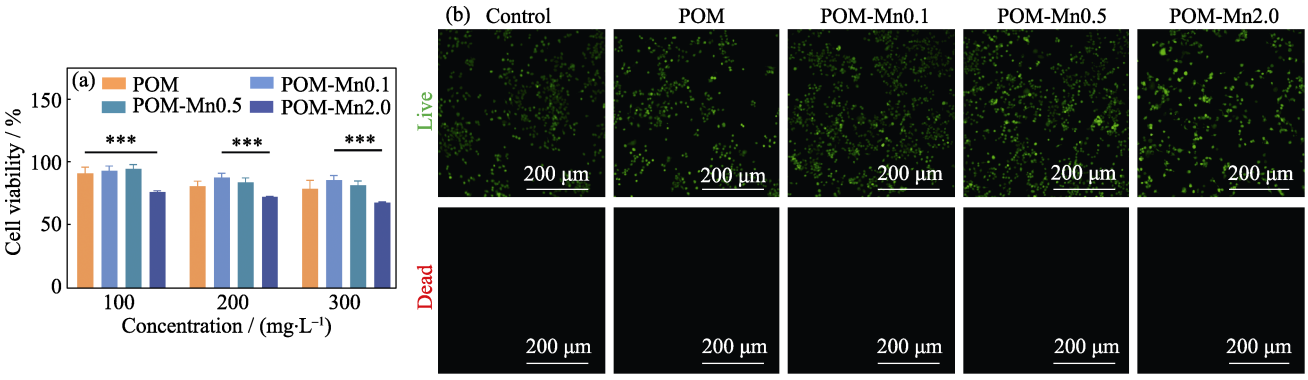

Fig. 5 (a) Cell viability and (b) live/dead staining images of RAW264.7 cells after being treated with POM, POM-Mn0.1, POM-Mn0.5, and POM-Mn2.0 (***: $p<0.001$)

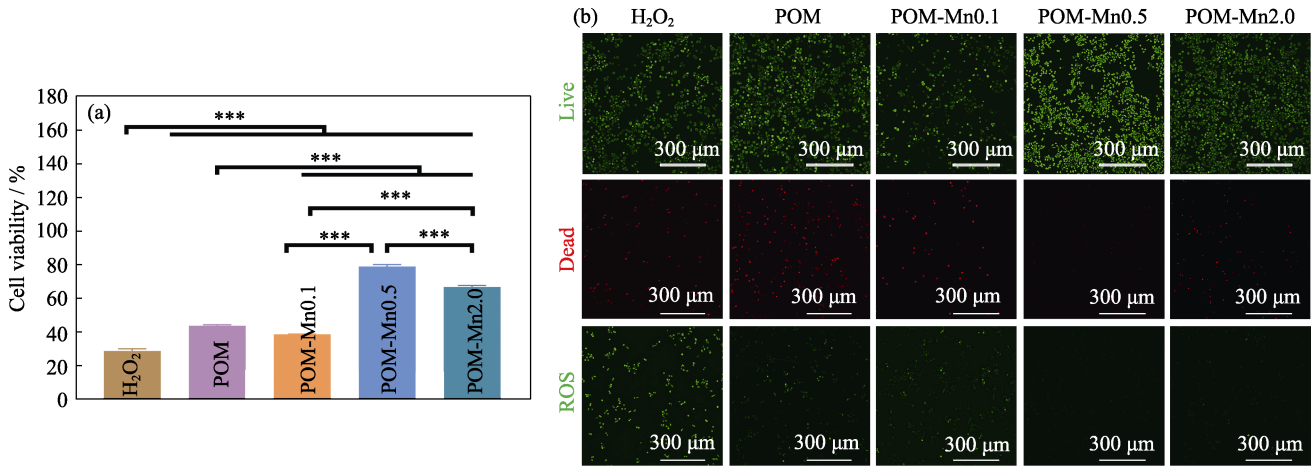

Fig. 6　(a) Cell viability and (b) live/dead staining images of H_2O_2-induced RAW264.7 cells after being treated with POM, POM-Mn0.1, POM-Mn0.5, and POM-Mn2.0 (***: p<0.001)

100, 200, and 300 mg/L, respectively, indicating cytotoxicity at higher doping levels. This cytotoxicity at high Mn doping levels may result from Mn overload impairing mitochondrial bioenergetics, such as reduced adenosine triphosphate production and respiratory function, leading to reduced macrophage viability at supraphysiological concentrations[12].

Nextly, the intracellular antioxidant capacity of POM-Mnx under oxidative stress conditions was evaluated. As shown in Fig. 6, under H_2O_2-induced oxidative stress, the cell viability of the blank control group (H_2O_2) is significantly reduced to (29.28±1.28)%. In contrast, RAW264.7 cells treated with POM, POM-Mn0.1, POM-Mn0.5, and POM-Mn2.0 exhibit viabilities of (44.30±0.65)%, (39.19±0.14)%, (79.54±1.17)%, and (67.37±0.96)%, respectively. In the experimental group of POM with a doping amount greater than or equal to 0.5, the number of live cells is significantly higher than the other three groups, while the fluorescence intensity of reactive oxygen species represented by DCFH-DA is lower. The order of anti-oxidative stress ability is POM-Mn0.5>POM-Mn2.0>POM>POM-Mn0.1, indicating that POM-Mn0.5 has excellent cytoprotective effects. In light of the fact that $\cdot O_2^-$ are more reactive than H_2O_2, the enhanced SOD-like activity of POM-Mn0.5 and POM-Mn2.0 significantly contributes to their superior cytoprotective effects. Moreover, POM-Mn0.5 exhibits elevated CAT-like activity, enabling more efficient decomposition of H_2O_2 and thereby preventing the downstream generation of superoxide radicals. This synergistic enzymatic activity culminates in the strongest antioxidative protection observed for POM-Mn0.5. These results substantiate that Mn doping markedly improves the cytoprotective capability of POM through simultaneous enhancement of both SOD- and CAT-like functions.

3　Conclusions

In summary, this study successfully prepared POM-Mnx and systematically investigated their structural, catalytic and cytoprotective properties. The incorporation of Mn into the framework led to notable structural changes. These structural modifications significantly enhanced their CAT-like and SOD-like enzyme activities, particularly at moderate Mn doping levels. The enhanced antioxidant enzyme activities translated into superior cytoprotective effects against oxidative stress in macrophages. Notably, the CAT-like activity of the POM-Mnx was found to be dependent on both Mn atoms and Mo=O, while the activity of the undoped and highly doped samples primarily originated from the Mo–O framework. These findings shed light on the structure-activity relationship in the doped materials and highlight their potential as promising antioxidant nanozymes for biomedical applications.

References:

[1] SIES H, BERNDT C, JONES D P. Oxidative stress. *Annual Review of Biochemistry*, 2017, **86:** 715.

[2] LI S, JIANG D, EHLERDING E B, *et al*. Intrathecal administration of nanoclusters for protecting neurons against oxidative stress in cerebral ischemia/reperfusion injury. *ACS Nano*, 2019, **13(11):** 13382.

[3] ZHANG C, BU W, NI D, *et al*. A Polyoxometalate cluster paradigm with self-adaptive electronic structure for acidity/reducibility-specific photothermal conversion. *Journal of the American Chemical Society*, 2016, **138(26):** 8156.

[4] WANG Y, WU Y, WANG Z, *et al*. Doping strategy and mechanism for oxide and sulfide solid electrolytes with high ionic conductivity. *Journal of Materials Chemistry A*, 2022, **10(9):** 4517.

[5] CHEN S, LU W, XU R, *et al*. Pyrolysis-free and universal synthesis of metal-NC single-atom nanozymes with dual catalytic

sites for cytoprotection. *Carbon*, 2023, **201:** 439.
[6] SHENG H X, LIN B Y, CHEN C Q, *et al*. From confined growth to enhanced peroxidase-like activity: nucleation of a phosphate-mediated Fe^{III}–Ce^{III}–oxo cluster inside the $\{P_8W_{48}\}$ nanoreactor. *Polyoxometalates*, 2024, **3(3):** 9140060.
[7] LIU Q, ZHANG Q, SHI W, *et al*. Self-assembly of polyoxometalate clusters into two-dimensional clusterphene structures featuring hexagonal pores. *Nature Chemistry*, 2022, **14(4):** 433.
[8] GUMEROVA N I, ROMPEL A. Polyoxometalates in solution: speciation under spotlight. *Chemical Society Reviews*, 2020, **49(21):** 7568.
[9] HARDCASTLE F D, WACHS I E. Determination of molybdenum–oxygen bond distances and bond orders by Raman spectroscopy. *Journal of Raman Spectroscopy*, 1990, **21(10):** 683.
[10] SUN Y, FAN W, LI Y, *et al*. Tuning coordination structures of Zn sites through symmetry-breaking accelerates electrocatalysis. *Advanced Materials*, 2024, **36(4):** 2306687.
[11] ZHANG X, LI G, CHEN G, *et al*. Single-atom nanozymes: a rising star for biosensing and biomedicine. *Coordination Chemistry Reviews*, 2020, **418:** 213376.
[12] WARREN E B, BRYAN M R, MORCILLO P, *et al*. Manganese-induced mitochondrial dysfunction is not detectable at exposures below the acute cytotoxic threshold in neuronal cell types. *Toxicological Sciences*, 2020, **176(2):** 446.

锰掺杂多金属氧酸盐增强活性氧清除能力用于细胞保护

曲博渲[1,2], 谭 继[1], 陈书寒[1], 刘宣勇[1]

(1. 中国科学院 上海硅酸盐研究所, 关键陶瓷材料全国重点实验室, 上海 200050; 2. 中国科学院大学 材料科学与光电工程中心, 北京 100049)

摘 要: 活性氧(ROS)的过量积累会导致细胞发生氧化应激而死亡。纳米酶是一类具有类似天然酶催化活性的纳米材料, 可清除 ROS 保护细胞免受氧化损伤。多金属氧酸盐(POMs)具有良好的氧化还原性和生物相容性, 是一种潜在的纳米酶材料, 但 POMs 较低的催化活性限制了其应用。本研究通过锰(Mn)掺杂策略有效增强了 Keggin 型 POMs ($[PMo_{12}O_{40}]^{3-}$)的类酶活性, 发现适量 Mn 掺杂可增强该 POMs 的类过氧化氢酶和类超氧化物歧化酶活性, 进而清除过量 ROS 保护细胞免受氧化应激损伤。本研究探讨了 Mn 掺杂水平、POMs 结构与催化活性之间的关系, 发现 Mn 与 Mo–O 框架之间的协同电子作用是增强其类过氧化氢酶活性的关键因素。本研究初步探索了 POMs 基纳米酶的优化设计策略, 研究结果可为抗氧化纳米酶的开发提供一定的科学参考。

关 键 词: 多金属氧酸盐; 氧化应激; 纳米酶; 催化医学

中图分类号: TQ171 **文献标志码:** A **文章编号:** 1000-324X(2026)06-0839-08